Nanoscale

PAPER

View Article Online
View Journal | View Issue

Cite this: *Nanoscale*, 2022, **14**, 8944

In situ probing the dynamic reconstruction of copper–zinc electrocatalysts for CO_2 reduction†

Yen-Po Huang,‡[a] Ching-Wei Tung,‡[a] Tai-Lung Chen,[a] Chia-Shuo Hsu,[a] Mei-Yi Liao,*[b] Hsiao-Chien Chen*[c,d] and Hao Ming Chen*[a,e]

Received 17th March 2022,
Accepted 2nd June 2022

DOI: 10.1039/d2nr01478e

rsc.li/nanoscale

Unravelling the dynamic characterization of electrocatalysts during the electrochemical CO_2 reduction reaction (CO_2RR) is a critical factor to improve the production efficiency and selectivity, since most pre-electrocatalysts undergo structural reconstruction and surface rearrangement under working conditions. Herein, a series of pre-electrocatalysts including CuO, ZnO and two different ratios of CuO/ZnO were systematically designed by a sputtering process to clarify the correlation of the dynamic characterization of Cu sites in the presence of Zn/ZnO and the product profile. The evidence provided by *in situ* X-ray absorption spectroscopy (XAS) indicated that appropriate Zn/ZnO levels could induce a variation in the coordination number of Cu sites *via* reversing Ostwald ripening. Specifically, the recrystallized Cu site with a lower coordination number exhibited a preferential production of methane (CH_4). More importantly, our findings provide a promising approach for the efficient production of CH_4 by *in situ* reconstructing Cu-based binary electrocatalysts.

Introduction

The excessive use of fossil fuels and massive emissions of carbon dioxide (CO_2) have led to an energy crisis and severe climate change.[1] Attention to energy- and environment-related issues has driven significant efforts in CO_2 conversion technologies.[2–4] The electrochemical CO_2 reduction reaction (CO_2RR) is emerging as a viable method to consume excess carbon dioxide in the atmosphere and store chemical energy in value-added chemicals.[5–7] Therefore, efforts have been devoted to exploring efficient electrocatalysts with high selectivity for the CO_2RR because CO_2 can be converted into formate, methanol (CH_3OH), methane (CH_4), ethylene (C_2H_4) ethanol (C_2H_5OH), *etc*. Among these, due to its relatively clean combustion in combustion engines,[8] high energy density and suitability to the present infrastructure for natural gas storage and transport,[9,10] the product of methane has shown significant economic benefits.

To date, Cu series catalysts such as oxide-derived Cu remain the most active catalysts for CO_2 reduction owing to the variety of their products and C_{2+} products based on the moderate binding energy between the Cu metal and the intermediates.[11,12] However, they exhibit poor selectivity towards hydrocarbons and normally produce CH_4 at a high cathodic potential. The pathway of reducing CO_2 to CH_4 should efficiently execute the protonation of CO under moderate binding energy, since weak binding energy results in the desorption of CO without any protonation process and strong binding energy causes significant overpotential. To this end, various Cu-based series of electrocatalysts had been investigated in terms of their particle size,[13] crystal orientation,[14,15] surface morphology,[16,17] and oxidation state.[3,18] Additionally, the strategy of preparing Cu-based alloys by introducing foreign particles into Cu tunes the binding energy between the intermediates and catalysts and thus alters the CH_4 distribution.[19]

Recently, a study on the *in situ* X-ray absorption spectroscopy (XAS) of Cu-based electrocatalysts suggested that the oxidation state of Cu electrocatalysts significantly influenced the CO_2RR pathway and product distribution.[3,18] In this, the production of C_{2+} hydrocarbons is highly correlated with the mixed Cu^+ and Cu^0 chemical state. Evidently, metallic Cu^0 favors methane production. However, Cu-based electrocatalysts are prone to self-oxidation in electrolytes and cannot get completely reduced to Cu metal even at high potentials. The presence of oxidized Cu-based electrocatalysts suppresses the production of C_{1+} hydrocarbons as well as reduces their selectivity. A previous study demonstrated that a Cu–Ag alloy prepared *via*

[a]*Department of Chemistry, National Taiwan University, Taipei 106, Taiwan. E-mail: haomingchen@ntu.edu.tw*
[b]*Department of Applied Chemistry, National Pingtung University, Pingtung 90003, Taiwan. E-mail: myliao@mail.nptu.edu.tw*
[c]*Center for Reliability Science and Technologies, Chang Gung University, Taoyuan 33302, Taiwan. E-mail: hc_chen@mail.cgu.edu.tw*
[d]*Kidney Research Center, Department of Nephrology, Chang Gung Memorial Hospital, Linkou, Taoyuan 33305, Taiwan*
[e]*National Synchrotron Radiation Research Center, Hsinchu 300, Taiwan*
†Electronic supplementary information (ESI) available. See DOI: https://doi.org/10.1039/d2nr01478e
‡These authors contributed equally.

the atomic interdiffusion of Ag into Cu nanowires stabilized metallic Cu^0 during the CO_2RR as well as inhibited its spontaneous reoxidation.[20] Besides, expanding the Cu–Cu distance through interdiffusion induced a stronger interaction with *CHO and thus accelerated CH_4 production.[21] In addition to the oxidation state, the Cu-based electrocatalyst coordination number also influences the product profile, which corresponds to the binding strength of the intermediate on the Cu nanoparticle surface.[22] A Cu electrocatalyst with a low coordination number inhibits C–C coupling; therefore, C_1 products dominate the product profile. As the coordination number of the Cu electrocatalyst gets close to 9, CH_4 is formed preferentially.[23] However, recent investigations involving in *in situ* XAS measurement have demonstrated that the coordination number of pre-electrocatalysts can change during electrocatalytic reactions such as water splitting and the CO_2RR.[24–30] This finding means that the correlation between the product and the coordination number of the electrocatalysts cannot be accurately confirmed if the electrocatalyst characterizations under working conditions cannot be captured immediately.

In this work, to unravel the effect of the dynamic coordination number of Cu on the selectivity of the CH_4 product in the duration of the CO_2RR, a Cu–Zn nanocomposite with various ratios was prepared *via* a sputtering process. The results indicate that the introduction of Zn in the optimal ratio significantly improved the production efficiency of CH_4. Furthermore, the *in situ* XAS results show that the dynamic coordination number of Cu sites strongly dominates the product profile, in which a decrease in the coordination number of the Cu sites is associated with an increase in the production efficiency of CH_4.

Results and discussion

Characterization of sputtering Cu–Zn nanocomposites

Fig. 1(a) shows a schematic diagram of the co-sputtering system with a Cu and ZnO target. Two conditions for preparing the Cu–Zn nanocomposites were adopted, wherein the total sputtering power was fixed at 200 W. The obtained samples were inspected by SEM-EDS to confirm the ratio of Cu and Zn. The sample obtained from a co-sputtering power of 50 W to the Cu target and 150 W to the ZnO target showed a particle size of around 500 nm (Fig. 1b). The EDS mapping and elemental composition results further confirm that Cu and Zn elements are homogeneously distributed on a gas diffusion layer (GDL) with an elemental composition ratio of 1 : 3 without noticeable phase separation (Fig. S1†); we thus named the sample s-$Cu_1Zn_3O_x$. Similarly, the sample with a rough surface from a sputtering power of 150 W to the Cu target and 50 W to the ZnO target showed an elemental composition ratio of 5 : 1, and was named s-$Cu_5Zn_1O_x$ (Fig. 1c). The crystalline structures of the deposited film were investigated by XRD (Fig. S2†). Sputtering Zn (s-ZnO) with a power of 200 W showed diffraction peaks at 2θ = 33.4° and 35.4°, corresponding to hexagonal wurtzite ZnO (JCP2) (card number, 003-0888). For sputtering Cu (s-CuO) with a power of 200 W, the characteristic diffraction peaks at 2θ = 34.7° and 37.7° were ascribed to the (−111) and (100) planes of cubic-structured CuO. The complete transformation of the metals to the metallic oxides ZnO and CuO was attributed to the exposure to the atmosphere after the sputtering process. Additionally, only the crystal features of ZnO and CuO were observed in s-$Cu_1Zn_3O_x$ and s-$Cu_5Zn_1O_x$, respectively, due to the lower mobility of the adatoms sputtered on the surface, which decreased the crystallinity.[31] Furthermore, the diffraction peaks of the bimetallic compounds monotonously shifted towards higher angles than those of s-ZnO and s-CuO. This phenomenon could show that the lower sputtering power of Cu in s-$Cu_1Zn_3O_x$ and Zn in s-$Cu_5Zn_1O_x$ induced lower compressive stress and lower lattice distortions.[32]

The chemical state and local structure of the sputtering samples were further probed by XAS, including X-ray absorption near-edge structure (XANES) and extended X-ray absorption fine structure (EXAFS). Fig. 2a shows the Zn K-edge XANES of s-ZnO, s-$Cu_1Zn_3O_x$ and s-$Cu_5Zn_1O_x$ along with the Zn foil and ZnO reference spectra. Compared with Zn foil, the Zn K-edge XANES of s-ZnO, s-$Cu_1Zn_3O_x$ and s-$Cu_5Zn_1O_x$ shifted to a higher energy. The oxidation states of s-ZnO, s-$Cu_1Zn_3O_x$ and s-$Cu_5Zn_1O_x$ were obtained from the maximum value of the first derivative of their respective XANES (Fig. 2b). The energies of the maximum values of s-ZnO and s-$Cu_1Zn_3O_x$ were close to that of the ZnO standard sample. Conversely, the value of s-$Cu_5Zn_1O_x$ is located between those of Zn foil and ZnO. According to the valency of zinc (either Zn(0) or Zn(II)), the extent of the oxidation state could be estimated using a mixture of Zn and ZnO in different proportions. However, the Fourier-transformed k^3-weighted EXAFS spectra of the Zn K-edge of s-ZnO, s-$Cu_1Zn_3O_x$ and s-$Cu_5Zn_1O_x$ only showed a Zn–O bond distance of 1.55 Å and a second coordination shell Zn–Zn bond distance of 2.87 Å without any Zn–Zn metallic bond, indicating that the value of s-$Cu_5Zn_1O_x$ being between those of Zn foil and ZnO was not caused by the mixed valency of Zn(0) and Zn(II) (Fig. 2c). This result also demonstrated that the Zn species existed in the form of ZnO in s-$Cu_5Zn_1O_x$. The fact that ZnO appeared to be below the oxidation state of +2 can be attributed to oxygen vacancies.[33,34] Additionally, no metallic bond of Zn–Cu was observed, implying that the co-

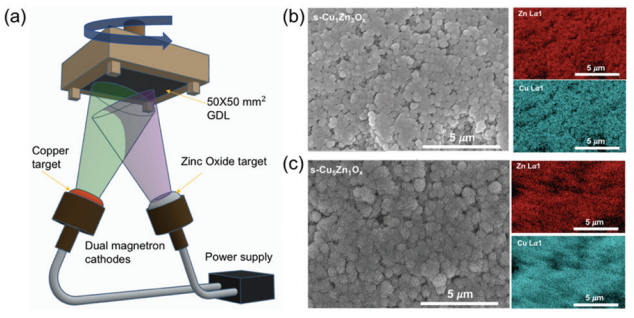

Fig. 1 (a) A schematic diagram of the co-sputtering system. SEM and EDS mapping of (b) s-$Cu_1Zn_3O_x$ and (c) s-$Cu_5Zn_1O_x$.

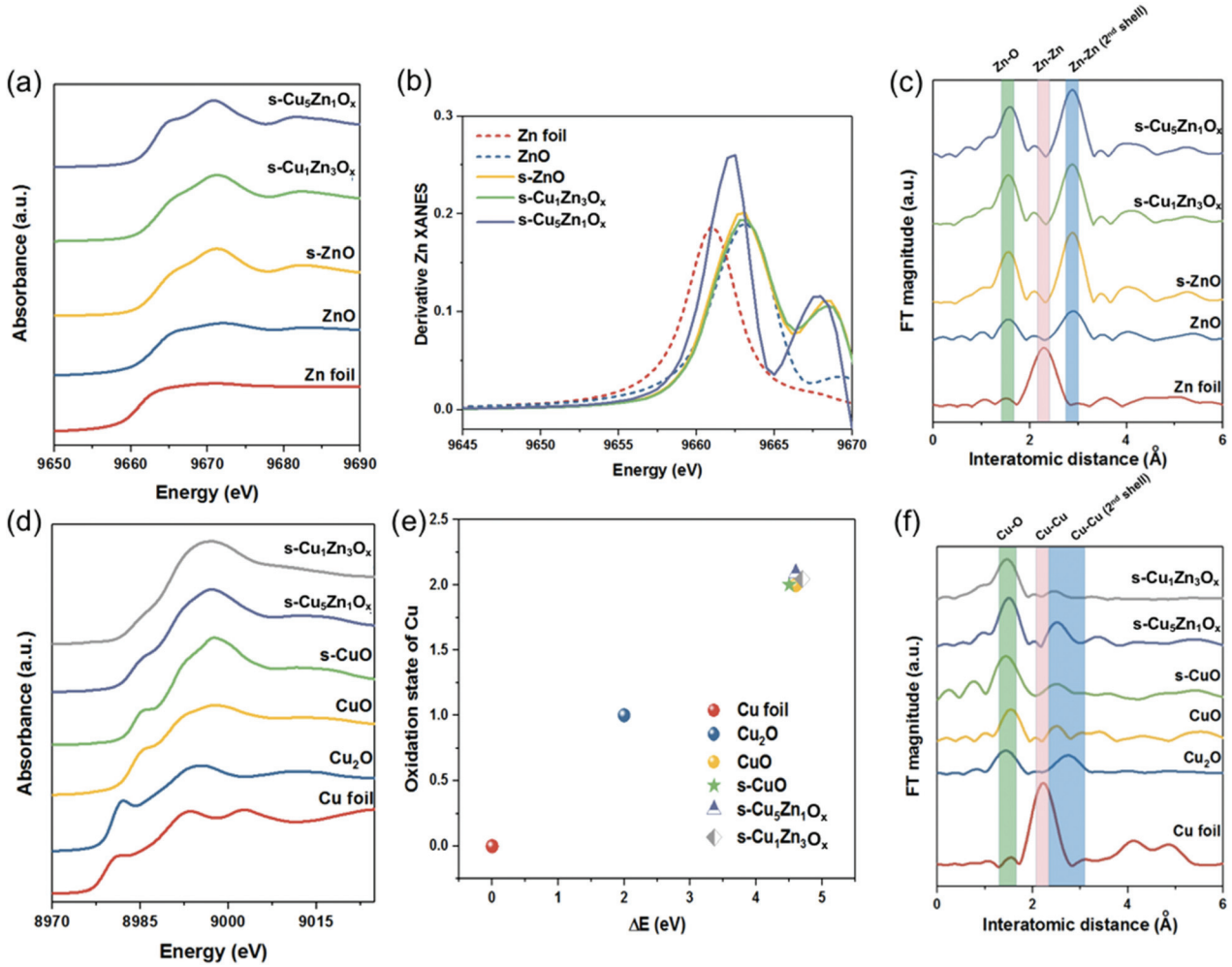

Fig. 2 (a) XANES spectra of the Zn K-edge, (b) their first derivative spectra and (c) their EXAFS spectra. (d) XANES spectra of the Cu K-edge, (e) their average oxidation states of Cu from the XANES spectra and (f) their EXAFS spectra.

sputtering samples did not form any alloy. Moreover, the Cu K-edge XANES of the sputtering samples shifted to a higher energy compared with that of Cu foil (Fig. 2d). By adopting a fitting procedure utilizing a linear combination of Cu, Cu_2O and CuO references (Fig. S3†), the oxidation states of Cu in the sputtering samples were all found to be +2, which was ascribed to the CuO structure (Fig. 2e). Besides, the co-sputtering samples showed the first and second coordination shells of the Cu–O and Cu–Cu scattering paths without observing a Cu–Zn bond. The results of XANES and *R* space analyses demonstrated that the co-sputtering Cu–Zn samples exhibited mixed structures of ZnO and CuO without forming any alloy. Additionally, the co-sputtering of ZnO and CuO could avoid the aggregation or overgrowth of individual metal oxides, which could afford well-dispersed smaller CuO and ZnO nanoparticles on the GDL. To clarify the coordination number with and without the co-sputtering process, EXAFS fitting of the prepared samples was carried out (Fig. S4†). Tables S1 and S2† show the structural parameters of the sputtered samples extracted from the Zn and Cu K-edge EXAFS. Compared with those of s-ZnO and s-CuO, the coordination number of co-sputtered ZnO/CuO was lower. Therefore, it could be deduced that the coordination number of the Cu site and Zn site could be reduced concurrently *via* the co-sputtering process.

Electrochemical performance for the CO_2RR

The electrocatalytic behaviors of the sputtering materials on the GDL for the CO_2RR were studied using linear sweep voltammetry (LSV) in a 1.0 M KOH solution under the flow of CO_2 (Fig. S5†). s-CuO/GDL achieved a CO_2RR current density higher than those of the other sputtering samples, implying that s-CuO/GDL had the highest CO_2RR activity. However, the activity decreased in the presence of ZnO. Fig. 3 and Fig. S6† show the product faradaic efficiency (FE) as a function of the applied iR-corrected potentials for various sputtering samples, with the corresponding product partial currents shown in Fig. S7.† In addition to hydrogen evolution, the C_1 products of CO and formate are the major products for s-ZnO, which is consistent with common ZnO nanoparticles or foil.[7] On the contrary, for s-CuO, the C_{2+} products of C_2H_4 and C_2H_5OH

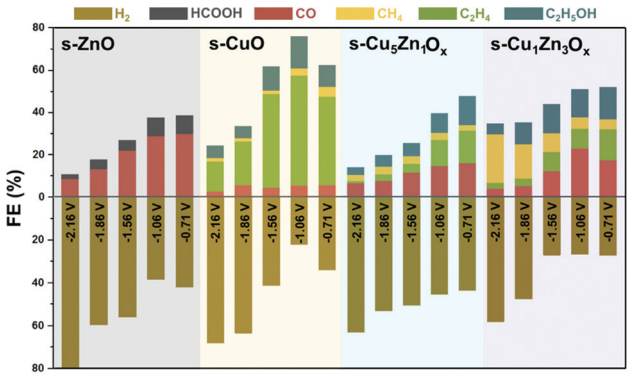

Fig. 3 Faradaic efficiency as a function of potential for various CO_2RR products.

dominated the reduction current in the range of −0.71 V and −2.16 V. However, the introduction of a small amount of ZnO ($s\text{-}Cu_5Zn_1O_x$) inhibited the activity of CuO, especially for the C_{2+} products. Compared with s-CuO, the total FE of the C_{2+} products dropped sharply and was replaced by CO as the main product, which was similar to the CO_2RR behavior of s-ZnO. Additionally, the FE of CH_4 on $s\text{-}Cu_5Zn_1O_x$ slightly increased at the applied potential from −1.56 V to −2.16 V compared with that on s-CuO, indicating that the introduction of Zn could improve the CH_4 production at an applied potential from −1.56 V to −2.16 V compared with that on s-CuO. This phenomenon was significantly amplified while the content of Zn increased to 75% in $s\text{-}Cu_1Zn_3O_x$, in which the production of C_{2+} products was strongly inhibited (Fig. 4a and b), and the partial current of CH_4 increased sharply (Fig. 4c). Fig. 4d clearly shows that the partial current ratio of C_{2+} products to CH_4 increased significantly with the increase in cathodic potential with the $s\text{-}Cu_1Zn_3O_x$ electrocatalyst. The stability of $s\text{-}Cu_1Zn_3O_x$ during the CO_2RR was confirmed by the variation in current at an applied potential of −1.86 V. As shown in Fig. S8,† no significant changes were observed over 50 h, indicating good electrocatalyst stability and good adhesion of the electrocatalyst on the GDL. Furthermore, the structural characterization of the electrocatalyst at 5 and 50 h of working time was performed by XPS. Although the *in situ* XAS demonstrated that the Cu site at −1.86 V was in the form of Cu^0, copper oxide and hydroxide were detected by the XPS spectrum of Cu 2p at both 5 h and 50 h, which could be ascribed to the effect of the alkaline electrolyte and the atmospheric environment. However, the Cu structure did not change between the sampling times of 5 and 50 h. This result shows that the electrocatalyst under working conditions was stable, leading to the stable current.

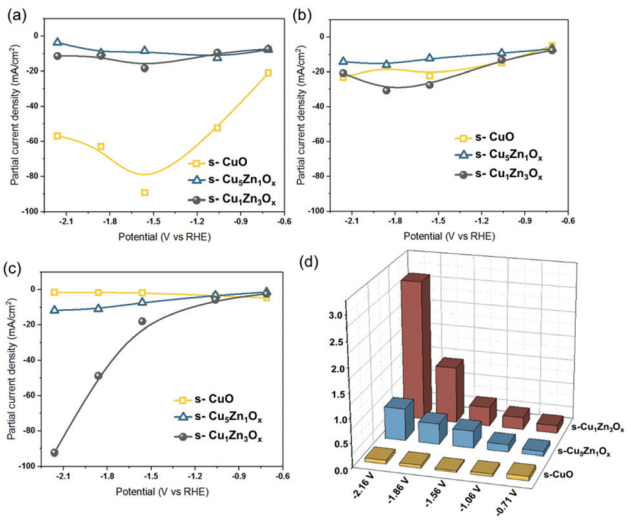

Fig. 4 (a) C_2H_4, (b) C_2H_5OH and (c) CH_4 partial current densities for s-CuO, $s\text{-}Cu_5Zn_1O_x$ and $s\text{-}Cu_1Zn_3O_x$ at different potentials. (d) CH_4/C_{2+} ratio as a function of potential for each sample.

In situ XAS probing of the dynamic electrocatalyst structure

It has been demonstrated that the oxidation state of Cu electrocatalysts inevitably undergoes dynamic changes as well as structural reconfigurations as the CO_2RR proceeds.[18,35] To reveal the correlation of the chemical state and the coordination environment to the product profile during the CO_2RR, *in situ* XAS of $s\text{-}Cu_5Zn_1O_x$ and $s\text{-}Cu_1Zn_3O_x$ was conducted (Fig. S9†). The Cu K-edge XANES of both $s\text{-}Cu_5Zn_1O_x$ and $s\text{-}Cu_1Zn_3O_x$ did not change while they were immersed in the electrolyte. By applying a potential of −1.06 V, the shift of energy towards a lower position was observed. The first derivative of XANES for both samples indicated that CuO was reduced and since then there was no further shift as the cathodic potential increased (Fig. 5a and S7a†). Fig. 5b shows the cathodic potential-dependent oxidation states of Cu in $s\text{-}Cu_5Zn_1O_x$ and $s\text{-}Cu_1Zn_3O_x$. The oxidation state of both samples immediately decreased from +2 to 0 when a potential

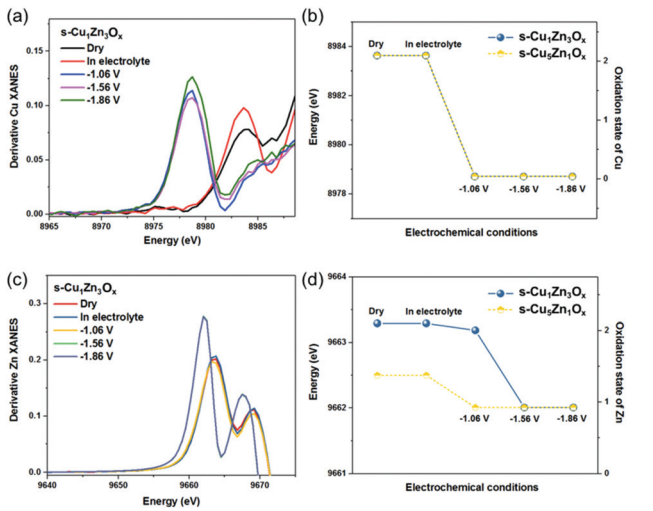

Fig. 5 (a) The first derivative spectra of the *in situ* Cu K-edge XANES of $s\text{-}Cu_1Zn_3O_x$. (b) The oxidation states of Cu in $s\text{-}Cu_1Zn_3O_x$ and $s\text{-}Cu_5Zn_1O_x$ under applied cathodic potential. (c) The first derivative spectra of the *in situ* Zn K-edge XANES of $s\text{-}Cu_1Zn_3O_x$. (d) The oxidation states of Zn in $s\text{-}Cu_1Zn_3O_x$ and $s\text{-}Cu_5Zn_1O_x$ under applied cathodic potential.

was applied at −1.06 V, which meant that the samples transformed from CuO to metallic Cu. However, the production of C_{2+} products was still observed at −1.6 V, even above this potential (Fig. 3). This result could be attributed to the spontaneous re-oxidation of Cu sites to maintain the oxidation state between 0 and +1, although the *in situ* XAS did not reveal this phenomenon. It should be noted that the potential-induced changes in the oxidation state of Zn showed dramatically different results (Fig. 5c, d and S10b†). The average oxidation state of s-$Cu_5Zn_1O_x$ decreased to +0.9 at −1.06 V and did not change further at higher cathodic potentials, indicating that most of ZnO was reduced to metallic Zn. However, ZnO in s-$Cu_1Zn_3O_x$ was hardly reduced to metallic Zn at −1.06 V, which could be due to the fact that the Zn sites spontaneously underwent another reduction reaction at this cathodic potential and induced auto-oxidation.

To further verify the changes in the local atomic environment of s-$Cu_5Zn_1O_x$ and s-$Cu_1Zn_3O_x$ during the CO_2RR, the Fourier-transformed k^3-weighted EXAFS spectra were recorded, and the structural parameters extracted from the *in situ* Cu and Zn K-edge EXAFS are summarized in Tables S3 to S6.† As mentioned previously, the most intense peak at ∼1.9 Å was attributed to a single scattering path of the Cu–O bond in s-$Cu_5Zn_1O_x$ and s-$Cu_1Zn_3O_x$. This peak disappeared at −1.06 V, and a new peak was observed at ∼2.5 Å, which was assigned to the first coordination shell of the Cu–Cu bond, indicating that the CuO structure in both samples was reduced to metallic Cu (Fig. S11 and S12†). Notably, no Cu–Zn bond was observed in both s-$Cu_5Zn_1O_x$ and s-$Cu_1Zn_3O_x$ during the CO_2RR, suggesting that the effect of the alloy structure on the product profile did not need to be considered. Moreover, Fig. 3 shows that the s-ZnO sample only produced CO and formate in the CO_2RR, which meant that the active site responsible for CH_4 production was the Cu site. The Cu–Cu and Zn–Zn distances of both samples increased negligibly with increasing potential (Fig. S13†). For the coordination environment of s-$Cu_5Zn_1O_x$, the coordination number of the Cu site slightly increased from 11.9 to 12.1 (Fig. 6a), and that of the Zn site remained unchanged (Fig. 6b). It is worth noting that the applied potential showed a strong correlation with changes in the coordination environment of the Cu and Zn sites of s-$Cu_1Zn_3O_x$, especially the Cu site, wherein the coordination number of the Cu site observably decreased from 11.9 to 10.9, while the potential increased from −1.06 V to 1.86 V. Furthermore, *in situ* XRD was used to further characterize the structural change of s-$Cu_1Zn_3O_x$ during the CO_2RR. As shown in Fig. S14,† the diffraction peaks of both CuO and ZnO disappeared accompanied by the formation of peaks at 2θ = 43.2° and 50.1°, which were ascribed to Cu (JCPDS No. 003-1018), indicating that CuO was electrochemically reduced to metallic Cu. Besides, the peak at 2θ = 43.2° was assigned to the metallic Zn (101) facet (JCPDS No. 87-0713). This result was consistent with the XAS observations for the Cu^{2+} to Cu^0 transition. These peaks of metallic Cu still existed without forming alloy peaks, while the potential increased to −1.56 V and −1.86 V. However, these peaks became broader with the increase in potential, meaning that the particle size of metallic Cu was reduced. Previous reports have shown that Cu atomic diffusion occurs during the CO_2RR. Both the dissolution of Cu from pristine nanoparticles and the electrochemical reduction of dissolved Cu lead to particle size reduction. Furthermore, the comparison of the particle size of s-$Cu_1Zn_3O_x$ before and after the CO_2RR at −1.86 V for 2 h was performed *via* TEM (Fig. S15†). Overall, the particle size of s-$Cu_1Zn_3O_x$ decreased slightly. The results of the *in situ* XAS, *in situ* XRD and TEM analyses reveal that the reconstruction of s-$Cu_1Zn_3O_x$ occurred during the CO_2RR through the dissolution–recrystallization of Cu, which reduced the coordination number as well as the particle size. This phenomenon could be described by reversing Ostwald ripening,[35,36] as shown in Fig. 7. The *in situ* XANES of the Zn k-edge showed that the white line intensity became stronger as cathodic potential was applied, which was attributed to the generation of oxygen defect structures. This n-type ZnO semiconductor improved the electron mobility of s-$Cu_1Zn_3O_x$,[37] which acted as the surfactant passivating surface of the Cu nanoparticles. Therefore, the surface energy of the Cu nanoparticles was decreased to negative.[38–40] In this case, the Cu nanoparticles exhibited a trend of increasing surface area-to-volume ratio with the dissolution of the larger size of the Cu site. Meanwhile, the cathodic potential was applied during the CO_2RR process, which was sufficient to electrochemically reduce the dissolved Cu ions. Additionally, similar to the reaction mechanism of zinc–copper batteries,[41] partially reduced metallic Zn acted as a reducing agent to reduce Cu ions, thus inducing the aforementioned auto-oxidation of the reduced Zn. Under these conditions, the recrystallization reaction of Cu was triggered, and the particle size of the newly formed Cu nanoparticles was forced to eventually reach a critical size. These processes caused a decrease in the coordination number of the Cu sites, which was consistent with the result

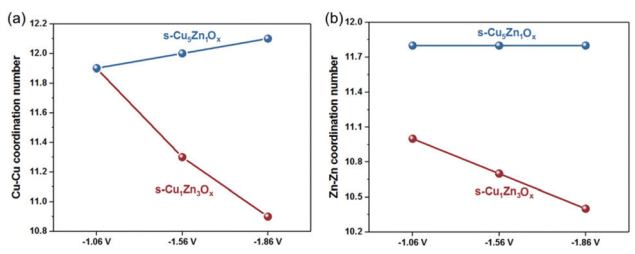

Fig. 6 Coordination number of the (a) Cu–Cu path and (b) Zn–Zn path as a function of potential for s-$Cu_1Zn_3O_x$ and s-$Cu_5Zn_1O_x$.

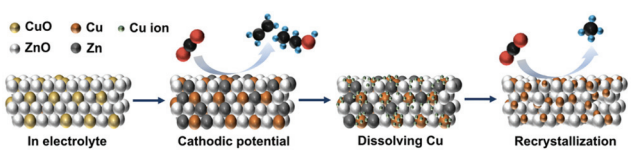

Fig. 7 Schematic process of the reconstruction of Cu sites during the CO_2RR.

of the *in situ* EXAFS. Besides, the EXAFS of the Cu and Zn K-edge of s-$Cu_1Zn_3O_x$ after an applied potential of −1.86 V were recorded. The EXAFS of the Cu and Zn K-edges of the post-electrocatalyst were similar to those at −1.86 V (Fig. S16†). Furthermore, the fitting results of the EXAFS showed ignorable changes in the coordination number and bond distance (Tables S3 and S5†), indicating that potential-induced dynamic reconstruction ceased when the potential was stopped. It also showed that the potential-induced structure was stable.

As the cathodic potential increased, a significant decrease in the coordination number of the Cu sites was noted along with a corresponding increase in CH_4 products and a decrease in C_{2+} products. This tendency is in agreement with a previous report that indicates that a lower coordination number of the Cu electrocatalyst suppresses the C–C coupling involved in C_{2+} products and improves the production of C_{1+} products.[22] However, a slight decrease in the coordination number of s-$Cu_1Zn_3O_x$ was also observed. According to the reaction mechanism of zinc–copper batteries, metallic Zn self-oxidizes into Zn ions while reducing Cu. This reaction also occurred in s-$Cu_1Zn_3O_x$ during the CO_2RR, where the reduced Zn site was converted into Zn ions at the same time as the dissolved Cu ions were reduced, subjecting Zn to a recrystallization process and slightly lowering the coordination number. With the assistance of the reduction potential and the reducing ability of metallic Zn, the oxidation state of the active Cu sites could be maintained at 0, which facilitated the production of CH_4.

Conclusions

In summary, a series of sputtering electrocatalysts were prepared to perform the CO_2RR. Although the introduction of s-ZnO into s-CuO decreased its activity in the CO_2RR, it significantly changed the product profile. Under optimal conditions, the production efficiency of CH_4 was clearly improved, and the C_{2+} products were suppressed. Furthermore, the results of *in situ* XAS reveal that CH_4 production was strongly dominated by the coordination number of the Cu sites, wherein the lower coordination number of the Cu sites formed CH_4 preferentially. The variation in the coordination number of Cu was attributed to the contribution of the Zn site, which triggered reversing Ostwald ripening during the CO_2RR. Meanwhile, besides the cathodic potential, the reduced Zn site also acted as a reducing agent to reduce dissolved Cu ions to carry out the recrystallization of the Cu sites. This work first unravelled the effect of the reversing Ostwald ripening/dynamic coordination number of Cu-based electrocatalysts for selective CH_4 production in the CO_2RR.

Experimental

Preparation of the gas diffusion electrodes (GDEs)

GDEs were fabricated by sputter deposition (oxide sputter). We used two targets (ZnO and Cu, 99.9% purity) sputtered using a Sigracet 39 BB GDL (Fuel Cell Store) with a surface area of 25 cm^2 to reach an almost 150 nm thickness. The sputtering power supply used four different factors (ZnO : Cu = 200 : 0, 150 : 50, 50 : 150, 0 : 200) kept at a total of 200 W DC in an atmosphere combined with 40 sccm Ar and 10 sccm O_2.

Electrochemical measurements

Electrochemical data were collected using a potentiostat (Autolab PGSTAT302N, Metrohm Autolab). In addition, we used a flow cell with three components composed of gas, cathode and anode chambers. The cathode and anode chambers were separated by an anion-exchange membrane (Fumasep FAA-3-PK-130, FuMA-Tech). Ag/AgCl (3 M KCl) was used as the reference electrode. Nickel foam was used as the anode. We chose 1 M KOH (ACROS) as the electrolyte. The catholyte and anolyte, both 40 ml, were circulated using a peristaltic pump at a rate of 30 rpm. To keep the cell in a CO_2 (Shen-Yi Gas Co.) environment, we used a mass flow meter (F-111BI, Bronkhorst High-Tech BV) to control the flow rate at 30 sccm. The product distribution was analyzed at various potentials by chronoamperometry. Linear sweep voltammetry (LSV) was carried out at a scan rate 10 mV s^{-1}, and potentiostatic electrochemical impedance spectroscopy (PEIS) was used to determine the uncompensated solution resistance (R_u).

CO_2 reduction reaction product analysis

The gaseous products were analyzed by online gas chromatography (Agilent 7890A, Agilent Technologies) using a thermal conductivity detector (TCD) for H_2 and CO quantitation and a flame ionization detector (FID) for CH_4 and C_2H_4 quantitation. HCOOH and ethanol were analyzed by NMR (Bruker AVIII HD-400 MHz NMR).

Characterization

Scanning electron microscopy (SEM, JEOL JEM-2100F) was used to characterize the surface morphology of the different Cu/Zn ratio GDEs, and energy-dispersive X-ray spectroscopy (EDX) line scans were conducted using an Oxford INCAx-act system to analyze the ratio of copper and zinc. X-ray diffraction (XRD, Bruker D2 Phaser) was used to obtain the crystalline structure using Cu Kα radiation (λ = 1.54 Å).

In situ quick-scanning X-ray absorption spectroscopy

The Cu and Zn K-edge absorption were measured using a TPS 44A, Hsinchu, Taiwan. The corresponding data were recorded in the total-fluorescence-yield mode. To obtain a high-quality spectrum, we applied the Quick-XAS mode with a time resolution of 5 seconds. The X-ray absorption experimental data were collected in the total-fluorescence-yield mode, in which the metallic Cu and Zn foil were taken as references for energy calibration.

Conflicts of interest

There are no conflicts to declare.

Acknowledgements

We acknowledge support from the Ministry of Science and Technology, Taiwan (Contracts No. MOST 108-2628-M-002-004-RSP, MOST 110-2113-M-153-001 and MOST 109-2222-E-182-002-MY3).

Notes and references

1 S. J. Davis, K. Caldeira and H. D. Matthews, *Science*, 2010, **329**, 1330–1333.
2 H. Y. Tan, S. C. Lin, J. Wang, C. J. Chang, S. C. Haw, K. H. Lin, L. D. Tsai, H. C. Chen and H. M. Chen, *ACS Appl. Mater. Interfaces*, 2021, **13**, 52134–52143.
3 J. Wang, H. Y. Tan, Y. Zhu, H. Chu and H. M. Chen, *Angew. Chem., Int. Ed.*, 2021, **60**, 17254.
4 Y. Zhu, T. R. Kuo, Y. H. Li, M. Y. Qi, G. Chen, J. Wang, Y. J. Xu and H. M. Chen, *Energy Environ. Sci.*, 2021, **14**, 1928.
5 X. Zhou, J. Shan, L. Chen, B. Y. Xia, T. Ling, J. Duan, Y. Jiao, Y. Zheng and S. Z. Qiao, *J. Am. Chem. Soc.*, 2022, **144**, 2079–2084.
6 Y. Xu, F. Li, A. Xu, J. P. Edwards, S. F. Hung, C. M. Gabardo, C. P. O'Brien, S. Liu, X. Wang, Y. Li, J. Wicks, R. K. Miao, Y. Liu, J. Li, J. E. Huang, J. Abed, Y. Wang, E. H. Sargent and D. Sinton, *Nat. Commun.*, 2021, **12**, 2932.
7 T. L. Chen, H. C. Chen, Y. P. Huang, S. C. Lin, C. H. Hou, H. Y. Tan, C. W. Tung, T. S. Chan, J. J. Shyue and H. M. Chen, *Nanoscale*, 2020, **12**, 18013.
8 M. Siegert, M. D. Yates, D. F. Call, X. P. Zhu, A. Spormann and B. E. Logan, *ACS Sustainable Chem. Eng.*, 2014, **2**, 910–917.
9 W. J. Zhang, Y. Hu, L. B. Ma, G. Y. Zhu, Y. R. Wang, X. L. Xue, R. P. Chen, S. Y. Yang and Z. Jin, *Adv. Sci.*, 2018, **5**, 1700275.
10 E. M. Nichols, J. J. Gallagher, C. Liu, Y. D. Su, J. Resasco, Y. Yu, Y. J. Sun, P. D. Yang, M. C. Y. Chang and C. J. Chang, *Proc. Natl. Acad. Sci. U. S. A.*, 2015, **112**, 11461.
11 L. Wu, K. E. Kolmeijer, Y. Zhang, H. An, S. Arnouts, S. Bals, T. Altantzis, J. P. Hofmann, M. C. Figueiredo, E. J. M. Hensen, B. M. Weckhuysen and W. V. D. Stam, *Nanoscale*, 2021, **13**, 4835–4844.
12 C. J. Chang, S. F. Hung, C. S. Hsu, H. C. Chen, S. C. Lin, Y. F. Liao and H. M. Chen, *ACS Cent. Sci.*, 2019, **5**, 1998–2009.
13 K. Manthiram, B. J. Beberwyck and A. P. Alivisatos, *J. Am. Chem. Soc.*, 2014, **136**, 13319–13325.
14 A. A. Peterson, F. A. Pedersen, F. Studt, J. Rossmeisl and J. K. Norskov, *Energy Environ. Sci.*, 2010, **3**, 1311.
15 W. Luo, X. Nie, M. J. Janik and A. Asthagiri, *ACS Catal.*, 2016, **6**, 219–229.
16 X. Zhou, J. Dong, Y. Zhu, L. Liu, Y. Jiao, H. Li, Y. Han, K. Davey, Q. Xu, Y. Zheng and S. Z. Qiao, *J. Am. Chem. Soc.*, 2021, **143**, 6681–6690.
17 Y. Li, F. Cui, M. B. Ross, D. Kim, Y. Sun and P. Yang, *Nano Lett.*, 2017, **17**, 1312–1317.
18 S. C. Lin, C. C. Chang, S. Y. Chiu, H. T. Pai, T. Y. Liao, C. S. Hsu, W. H. Chiang, M. K. Tsai and H. M. Chen, *Nat. Commun.*, 2020, **11**, 3525.
19 X. Wang, P. Ou, J. Wicks, Y. Xie, Y. Wang, J. Li, J. Tam, D. Ren, J. Y. Howe, Z. Wang, A. Ozden, Y. Z. Finfrock, Y. Xu, Y. Li, A. S. Rasouli, K. Bertens, A. H. Ip, M. Graetzel, D. Sinton and E. H. Sargent, *Nat. Commun.*, 2021, **12**, 3387.
20 C. J. Chang, S. C. Lin, H. C. Chen, J. Wang, K. J. Zheng, Y. Zhu and H. M. Chen, *J. Am. Chem. Soc.*, 2020, **142**, 12119–12132.
21 D. Y. Shin, J. H. Jo, J. Y. Lee and D. H. Lim, *Comput. Theor. Chem.*, 2016, **1083**, 31–37.
22 R. Reske, H. Mistry, F. Behafarid, B. R. Cuenya and P. Strasser, *J. Am. Chem. Soc.*, 2014, **136**, 6978–6986.
23 K. J. P. Schouten, Z. Qin, E. P. Gallent and M. T. M. Koper, *J. Am. Chem. Soc.*, 2012, **134**, 9864.
24 D. Yao, C. Tang, A. Vasileff, X. Zhi, Y. Jiao and S. Z. Qiao, *Angew. Chem., Int. Ed.*, 2021, **60**, 18178–18184.
25 H. Sun, C. W. Tung, Y. Qiu, W. Zhang, Q. Wang, Z. Li, J. Tang, H. C. Chen, C. Wang and H. M. Chen, *J. Am. Chem. Soc.*, 2022, **144**(3), 1174–1186.
26 J. Wang, H. Y. Tan, T. R. Kuo, S. C. Lin, C. S. Hsu, Y. Zhu, Y. C. Chu, T. L. Chen, J. F. Lee and H. M. Chen, *Small*, 2021, **17**, 2005713.
27 Y. Zhu, J. Wang, H. Chu, Y. C. Chu and H. M. Chen, *ACS Energy Lett.*, 2020, **5**, 1281.
28 H. C. Chen, T. L. Chen, S. C. Lin, C. S. Hsu, T. S. Chan, M. Y. Liao and H. M. Chen, *ChemCatChem*, 2020, **20**, 1926.
29 S. F. Hung, Y. Zhu, G. Q. Tzeng, H. C. Chen, C. S. Hsu, Y. F. Liao, H. Ishii, N. Hiraoka and H. M. Chen, *ACS Energy Lett.*, 2019, **4**, 2813.
30 J. Gu, C. S. Hsu, L. Bai, H. M. Chen and X. Hu, *Science*, 2019, **364**, 1091.
31 K. Y. Chan and B. S. Teo, *Microelectron. J.*, 2007, **38**, 60–62.
32 K. H. Ri, Y. Wang, W. L. Zhou, J. X. Gao, X. J. Wang and J. Yu, *Appl. Surf. Sci.*, 2011, **258**, 1283–1289.
33 H. Liu, Y. Wang, J. Wu, G. Zhanga and Y. Yan, *Phys. Chem. Chem. Phys.*, 2015, **17**, 9098–9105.
34 P. Ticali, D. Salusso, R. Ahmad, C. A. Sam, A. Ramirez, G. Shterk, K. A. Lomachenko, E. Borfecchia, S. Morandi, L. Cavallo, J. Gascon, S. Bordiga and U. Olsbye, *Catal. Sci. Technol.*, 2021, **11**, 1249–1268.
35 N. T. K. Thanh, N. Maclean and S. Mahiddine, *Chem. Rev.*, 2014, **114**(15), 7610–7630.
36 V. M. Burlakov and A. Goriely, *Appl. Sci.*, 2020, **10**, 5359.
37 X. Wang, K. Xu, X. Yan, X. Xiao, C. Aruta, V. Foglietti, Z. Ning and N. Yang, *ACS Appl. Mater. Interfaces*, 2020, **12**, 8403–8410.
38 R. van den Berg, T. E. Parmentier, C. F. Elkjær, C. J. Gommes, J. Sehested, S. Helveg, P. E. de Jongh and K. P. de Jong, *ACS Catal.*, 2015, **5**, 4439–4448.
39 N. T. K. Thanh, N. Maclean and S. Mahiddine, *Chem. Rev.*, 2014, **114**, 7610–7630.
40 J. R. Shimpi, D. S. Sidhaye and B. L. V. Prasad, *Langmuir*, 2017, **33**, 9491–9507.
41 Q. Zhu, M. Cheng, B. Zhang, K. Jin, S. Chen, Z. Ren and Y. Yu, *Adv. Funct. Mater.*, 2019, **29**(50), 1905979.

